Tribology International 198 (2024) 109851

Contents lists available at ScienceDirect

Tribology International

journal homepage: www.elsevier.com/locate/triboint

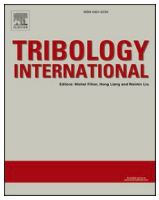

Analysis of the tribological behaviour of the lubricated contacts of a connecting rod equipped with a direct pin oiling gallery

Valerio Mangeruga [a,1], Saverio Giulio Barbieri [a,*,2], Matteo Giacopini [a,3], Luigi Bianco [a,4], Andrea Ferretti [b], Michele Mazziotta [b]

[a] University of Modena and Reggio Emilia, Engineering Department "Enzo Ferrari", Via Vivarelli 10, 41125 Modena, Italy
[b] Ducati Motor Holding, Engine Simulation Department, Via Antonio Cavalieri Ducati, 3, 40132 Bologna, Italy

ARTICLE INFO

Keywords:
Elastohydrodynamic
Direct pin oiling gallery port
Connectig rod
Experimental, Evidence

ABSTRACT

This paper describes a methodology for identifying a suitable design of a Direct-Pin-Oiling (DPO) gallery, drilled through the conrod shank of a high-performance internal combustion engine, to directly supply pressurized lubricant to the piston pin/small-end interface. Initially, a multibody elastohydrodynamic model is set up to analyse the tribological behaviour of conrod bearings, when considering a standard configuration employing a passive lubricating hole drilled on the top of the small-end. Then, a preliminary DPO gallery is introduced to examine how it affects the oil flows at lubricated interfaces and their tribological behaviour. The numerical results and parallel experimental evidence underline the need to modify the initial configuration of the DPO gallery and a more performing gallery design is proposed.

1. Introduction

During the early stages of the design process of internal combustion engine components, it is particularly advantageous to be able to accurately predict the tribological behaviour of the different lubricated joints [1,2]. One of the first things to define, but also one of the hardest to change, is the general configuration of the engine bearings, i.e. the location and size of the oil supply holes and/or the bearing size [3,4]. The development of a predictive simulation model can offer a solid justification for the designer's decisions in order to reduce friction losses and avoid excessive wear of sliding joints [5].

In this scenario, lubrication problems could arise, especially regarding the conrod small-end, when considering a high maximum engine speed [6]. In fact, the standard passive holes drilled on the upper part of the conrod small-end may not guarantee a high enough oil flow for a continuous supply of the interface, thus possibly reducing the performance of the hydrodynamic bearing [7,8]. Actually, the addition of a specific Direct-Pin-Oiling (DPO) gallery is conceivable, which is usually obtained by Electric Discharge Machining (EDM) and runs through the conrod shank from the big-end to the small-end to increase the amount of oil reaching the piston pin/small-end interface [9,10], see Fig. 1. However, the introduction of this additional gallery could lead to wear problems in the conrod big-end bearing when an excessive amount of supply oil is bled towards the small-end or due to the perturbation introduced on the mating surface of the connecting rod bearings by the feed holes of the DPO gallery. Therefore, the correct prediction of these phenomena is mandatory in order not to jeopardize the efficiency of the crank mechanism. In 2006, Ligier and Ragot [11] studied the influence of the layout of the passive holes located on the small-end bearing on the lubrication performance. In 2021, Du et al. [12] tried to optimize the performance of the main bearing modifying the profile without considering the influence of possible oil galleries. In 2023, Yin et al. [13] analysed comprehensively the tribo-dynamic behaviour of a conrod small-end in the presence of a DPO gallery port. In the present contribution, a numerical methodology is first presented and then used to discuss the design of a DPO gallery. Specifically, the lubricated contacts

* Corresponding author.
E-mail addresses: valerio.mangeruga@unimore.it (V. Mangeruga), saveriogiulio.barbieri@unimore.it (S.G. Barbieri), matteo.giacopini@unimore.it (M. Giacopini), luigi.bianco@unimore.it (L. Bianco), andrea.ferretti@ducati.com (A. Ferretti), michele.mazziotta@ducati.com (M. Mazziotta).
[1] ORCID 0000-0002-2133-4881.
[2] ORCID 0000-0002-2736-2664.
[3] ORCID 0000-0002-3644-5541.
[4] ORCID 0000-0001-5426-9492.

https://doi.org/10.1016/j.triboint.2024.109851
Received 21 February 2024; Received in revised form 21 May 2024; Accepted 4 June 2024
Available online 6 June 2024

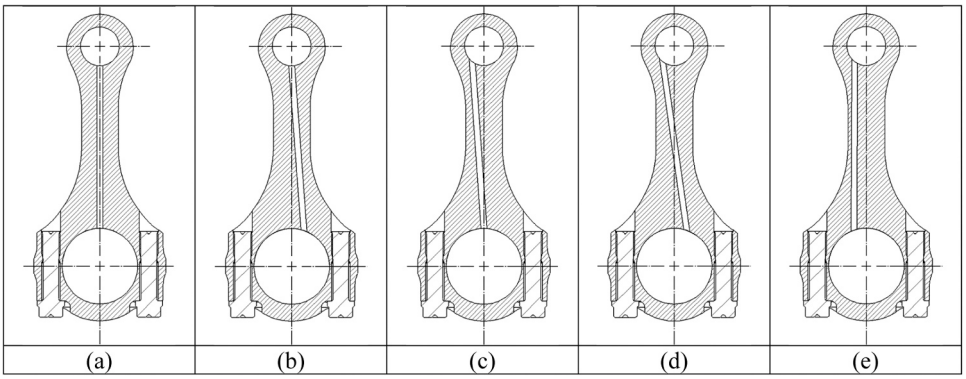

Fig. 1. Different possible configurations of the DPO gallery.

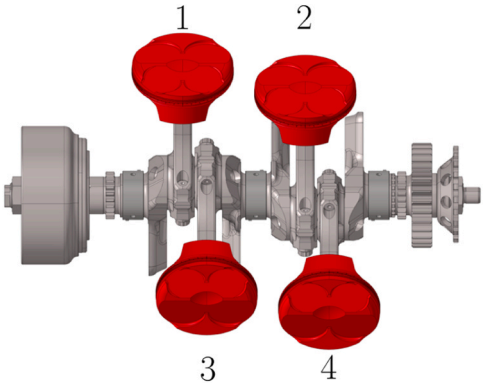

Fig. 2. Schematic of the components involved in the multibody analyses.

Table 1
Main parameters of the Craig-Bampton condensations.

Description	Number of elements	Number of condensed nodes	Number of condensed modes	Rayleigh damping parameters	
				Frequency [Hz]	Damping Ratio [-]
Gudgeon pin	12,240	11	80	F1 = 500 F2 = 1000	d1 = 0.03 d2 = 0.05
Connrod	154,207	496	80	F1 = 500 F2 = 1000	d1 = 0.05 d2 = 0.1
Crankshaft	865,306	53	80	F1 = 500 F2 = 1000	d1 = 0.03 d2 = 0.05

at the conrod small-end towards the gudgeon pin, and at the conrod big-end towards the crank pin are evaluated, while the lubricant flow promoted by the DPO gallery is monitored.

In particular, the paper is structured as follows. First, preliminary notions are provided. Then, the original conrod is considered. The DPO gallery is not present, and the component is studied through multibody analyses to estimate its performance. The results are presented focusing on the tribological behaviour of the two plain bearings of the conrod and on the corresponding oil flows. Next, the DPO gallery is inserted, a second multibody analysis is performed, and the oil flow and contact pressures are compared to the initial configuration. Experimental data collected during the preliminary engine bench tests are also presented and used to validate the numerical predictions. Based on these results, a more suitable configuration of the DPO gallery is proposed. The results of additional multibody analyses are provided to demonstrate the improvements offered by the modified layout. Observations after experimental tests conducted on the connecting rods with the modified DPO gallery are also shown. Finally, some conclusions end the document.

The authors acknowledge that some of the numerical results presented in this contribution have been concealed or normalized for reasons of company confidentiality.

2. Multibody models

2.1. Generic model set-up

Multibody simulations have been performed to quantify the effect of introducing the DPO gallery. Different connecting rod designs have been analysed, with and without the DPO gallery, while the engine system has been kept the same in the different simulations.

Specifically, the engine examined is a high-performance, four-stroke, four-cylinder V-Type engine. Fig. 2 shows the conventional numbering of the crank mechanisms. In particular, conrods 1 and 3 are connected to one crank pin while conrods 2 and 4 are linked to the other crank pin. It is important to point out that the same connecting rod geometry is adopted for all cylinders. This is an important aspect to consider when designing the DPO gallery. All simulations have been performed at the maximum engine speed of 16500 rpm.

For the description of the elastic-dynamic behaviour of the various components involved, a modal reduction based on the Craig-Bampton [14,15] component mode synthesis approach has been used adopting Altair Optistruct. The first 80 modes have been condensed for each component. A preliminary sensitivity analysis has been performed to identify the suitable number of modes that would provide accurate results without being unnecessarily burdensome from a computational point of view. Table 1 shows the main parameters of the condensations. Regarding the gudgeon pin, 11 nodes along the pin axis have been selected, 6 in correspondence with the piston bosses interface and 5 in correspondence with the conrod small-end. These nodes represent the master nodes of different spiders of rigid elements (RBE3) linked to the external surface of the pin. Then, for the condensation of the connecting rod, 496 interface nodes have been identified: 240 nodes (48 circumferential, 5 axial) at the inner surface of the small-end, 240 nodes (48 circumferential, 5 axial) at the inner surface of the big-end and 16 nodes on the side planar surfaces of the big-end. Finally, 53 nodes have been selected for the crankshaft: 20 along the crankpin axes, 15 along the main journal axes, 16 on the planar surfaces of the axial thrust bearing, 1 in correspondence with the output gear and 1 on the other side of the shaft to link the inertia of a non-discretized gear. Again, the nodes along the pin and journal axes represent the master nodes of different spiders of rigid elements (RBE3) linked to the external surface of the pins.

Excite Power Unit [16] has been employed for the multibody simulations. Fig. 3 shows the layout of the model. To connect the different components, suitable joints have been used as detailed in the following:

- Four EHD2 joints (elastohydrodynamic bearing) have been used to simulate the interfaces between conrods 1 and 3 and their related

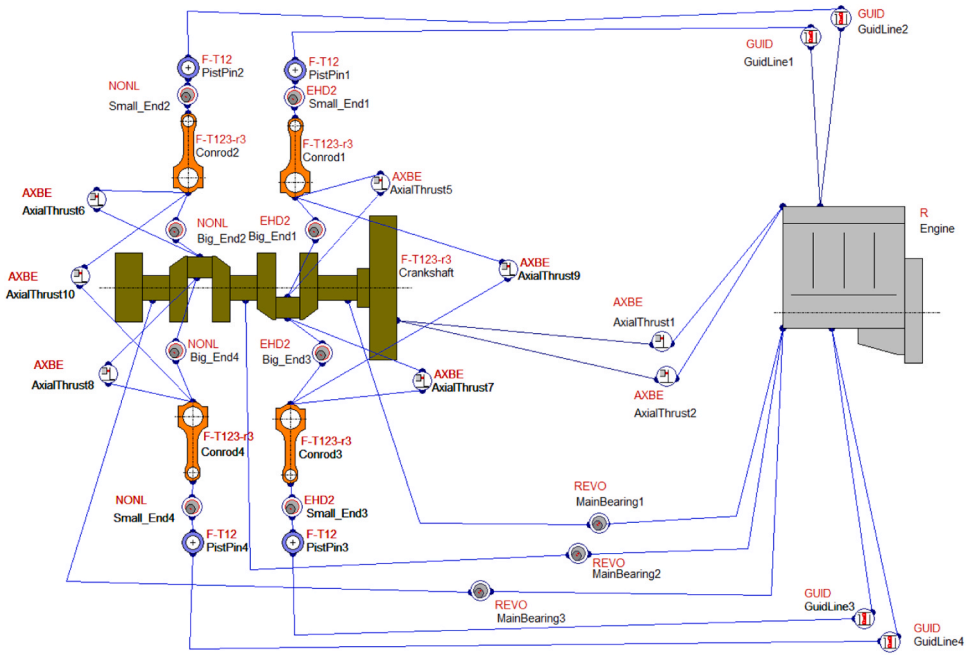

Fig. 3. The layout of the Excite Power Unit multibody model.

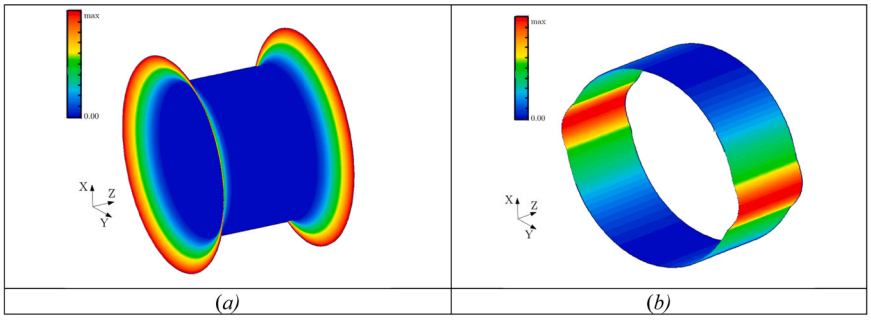

Fig. 4. Radial perturbation of conrod bearings: (a) small-end bushing barrel shape; (b) big-end bearing lemon shape.

Table 2
Measured/estimated parameters for Greenwood/Tripp asperity contact model.

Small-end parameters			Big-end parameters			Unit
Piston bosses mean summit height - δ_{s1}	measured	0.965	Big-end bearing mean summit height - δ_{s1}	estimated [19]	0.8	μm
Gudgeon pin mean summit height of - δ_{s2}	measured	0.876	Crankpin mean summit height of - δ_{s2}	estimated [19]	0.1	μm
Total mean summit height - δ_s	$\delta_{s2} + \delta_{s2}$	1.219	Total mean summit height - δ_s	$\delta_{s2} + \delta_{s2}$	1.125	μm
Piston bosses root-Mean-Square of summit height - σ_{s1}	measured	0.593	Big-end bearing root-Mean-Square of summit height - σ_{s1}	estimated [19]	1	μm
Gudgeon pin root-Mean-Square of summit height - σ_{s2}	measured	0.626	Crankpin root-Mean-Square of summit height - σ_{s2}	estimated [19]	0.125	μm
Total root-Mean-Square of summit height - σ_s	$\sqrt{\sigma_{s1}^2 + \sigma_{s2}^2}$	1.303	Total root-Mean-Square of summit height - σ_s	$\sqrt{\sigma_{s1}^2 + \sigma_{s2}^2}$	0.806	μm
Elastic factor - K	$\frac{16\sqrt{2\pi}}{15}(\sigma_s\beta\eta)^2\sqrt{\frac{\sigma_s}{\beta}}$	0.00491	Elastic factor - K	$\frac{16\sqrt{2\pi}}{15}(\sigma_s\beta\eta)^2\sqrt{\frac{\sigma_s}{\beta}}$	0.003	-
Composite elastic modulus - E^*	$\frac{1}{\left(\frac{1-\nu_1^2}{E_1}+\frac{1-\nu_2^2}{E_2}\right)}$	115,384.6	Composite elastic modulus - E^*	$\frac{1}{\left(\frac{1-\nu_1^2}{E_1}+\frac{1-\nu_2^2}{E_2}\right)}$	115,384.6	MPa

gudgeon pins and crank pin. The mass-conserving cavitation model proposed by Elrod and Adams is employed to solve the hydrodynamic problem [17,18]. A regular structured fluid mesh has been defined. Referring to the small-end, 65 nodes along the axis and 192 nodes on the circumferential direction have been used. Considering the big-end, 65 nodes along the axis and 384 nodes on the circumferential direction have been employed. An operating temperature of 130 °C has been considered in the model to account for the variation of the oil properties as a function of temperature. Elastic deformations of contacting bodies are taken from the interaction of the fluid meshes with the condensed nodes of conrods, crankshaft and piston pins (note that the fluid meshes have been defined as multiples of the condensed nodes to facilitate the interpolation process [16]).

Geometric details have been included in the description of these

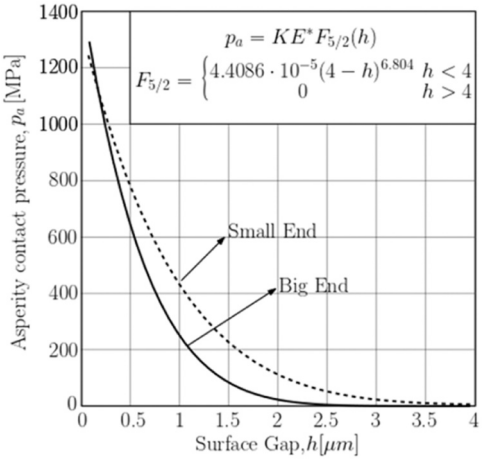

Fig. 5. Greenwood-Tripp curves for the asperity contact model.

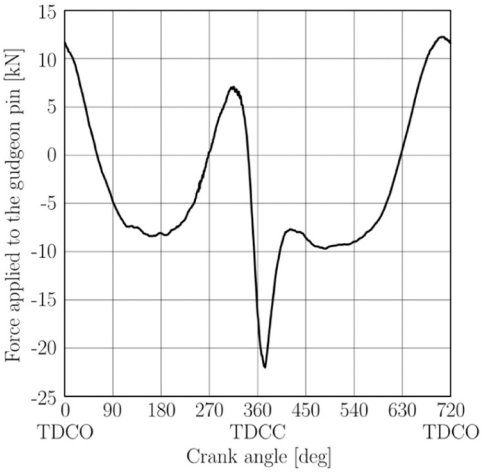

Fig. 6. The force applied to the gudgeon pin as a function of the crank angle, conrod 1.

bearings. In particular, the barrel shaped [19,20] geometry of the conrod small-end bushing has been implemented, see Fig. 4(a), and the specific lemon shape profile [21] has been considered for the inner surface of the big-end bearing, see Fig. 4(b). The legend has been concealed for confidentiality reasons. Geometric distortions due to the bearing assembly have been neglected.

Furthermore, the Greenwood/Tripp model [22–24] has been adopted to govern possible asperity contact occurrences in these joints. The required properties have been obtained using the measured/estimated parameters of Table 2 and following the methodology proposed in [25]. Fig. 5 shows the derived Greenwood/Tripp curves for both the small-end and big-end interfaces.

- A simplified approach has been instead adopted for conrod 2 and 4. In fact, to estimate the effect of the DPO gallery, it is sufficient to study in detail the hydrodynamic behaviour of conrods 1 and 3, while the influence of the other crank mechanisms involved is marginal. Therefore, the cylindrical contacts of conrods 2 and 4 have been modelled using NONL (non-linear spring/damper) joints to avoid excessively increasing the complexity of the model and to save computational time. The NONL joint is a set of non-linear springs/dumpers that simulates in a simplified manner the interaction between the big-end and the crankshaft and the small-end and the piston pin, connecting the nodes at the inner surfaces of the conrod bearings to the corresponding nodes along pin and crankshaft axes. The non-linear stiffness has been defined in a way to avoid that, when the maximum load insists on the coupling, the radial displacement is higher than the bearing radial gap.
- REVO joints have been used to connect the crankshaft to a rigid engine block to mimic the rotary coupling. Nodes condensed along crankshaft main journals have been used and the non-linear radial stiffness of these REVO joints has been defined similarly as for the NONL joints.
- The pistons have not been included in the model and four GUID (piston-liner guidance) joints have been set up to directly connect the piston pin to the cylinder liner, mimicking the piston-liner interaction. Nodes condensed along the pin axes in correspondence with the piston bosses have been used for this purpose. Moreover, the loadings typically transmitted by the piston have been applied directly to the same condensed nodes of the gudgeon pin. Fig. 6 depicts the resultant force ascribed to the piston as a function of the crank angle accounting for contributions of both combustion forces and piston alternating inertial forces.
- AXBE (axial thrust bearing) joints have been used to uniquely define the position of the crankshaft and connecting rods along a direction parallel to the crankshaft axis.
- The OSL (oil supply line) joint has been inserted to model the DPO gallery of conrod 1 and 3 in those simulations where the DPO is present. The Bernoulli equation and the continuity equation for pipes with constant cross sections are applied between the big-end hole and small-end hole of each DPO gallery:

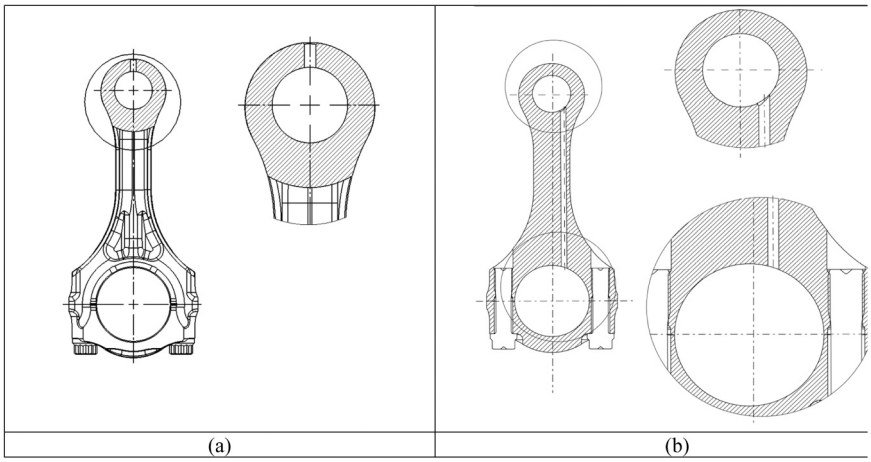

Fig. 7. Oil supply of conrod small-end: (a) radial through hole; (b) DPO gallery.

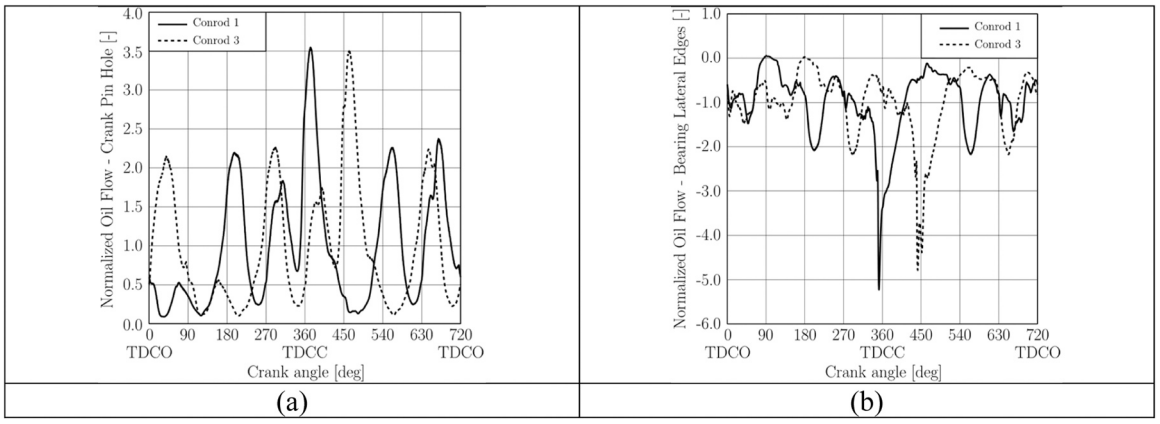

Fig. 8. Normalized oil flow in the big-end bearing of conrods 1 and 3 without the DPO gallery: (a) crank pin hole; (b) bearing lateral edges.

Table 3
Normalized average oil flows in the conrod big-end bearings with and without DPO gallery.

	Normalized average flow of oil out of the crankshaft feeding hole		Normalized average flow of oil passing directly from the crankshaft feeding hole into the DPO gallery	Normalized average flow of oil remaining in the bearing	Normalized average flow of oil passing from the bearing into the DPO gallery	Normalized average flow of oil out of the edges of the bearing	
	Without DPO gallery	With DPO gallery	With DPO gallery	With DPO gallery	With DPO gallery	Without DPO gallery	With DPO gallery
Conrod 1	1	1.0710	0.0555	1.0155	-0.0592	-1	-0.9563
Conrod 3	1	1.0756	0.0628	1.0128	-0.0569	-1	-0.9559

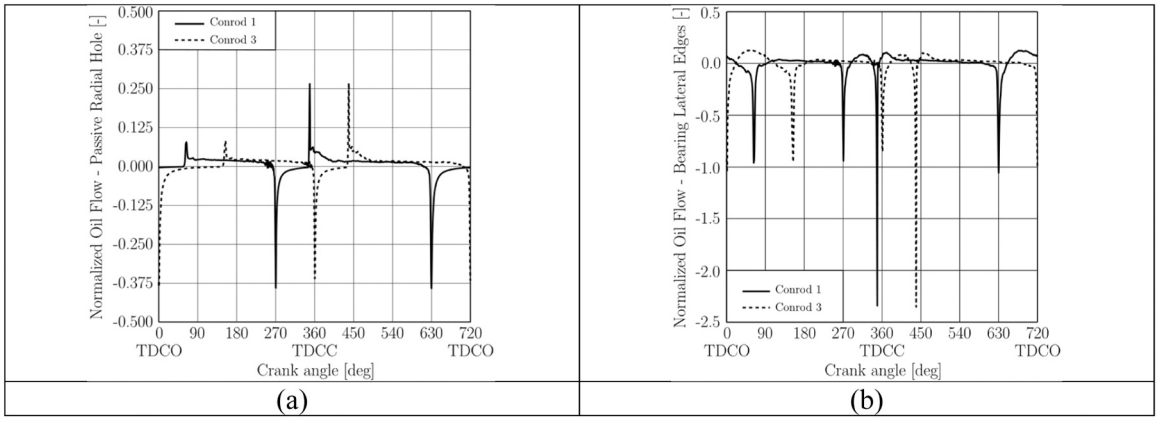

Fig. 9. Normalized oil flow in the small-end bearing of conrods 1 and 3 without the DPO gallery: (a) passive radial hole; (b) bearing lateral edges.

Table 4
Normalized average oil flows in the conrod small-end bearings with and without DPO gallery.

	Normalized average flow of oil from oil supply hole		Normalized average flow of oil out of the edges of the bearing	
	WithoutDPO gallery	With DPO gallery	WithoutDPO gallery	With DPO gallery
Conrod 1	0.0042	0.1147	-0.0042	-0.1147
Conrod 3	0.0042	0.1197	-0.0042	-0.1197

$$\left(\rho\frac{w^2}{2}+p\right)\Big|_{small-enf}^{big-end}+Y_{big-end,small-end}+\Delta p_{gyros}^{straight}= \quad 0 \tag{1}$$

where ρ, w and p are the density, the velocity of the lubricant and the pressure of the lubricant respectively; $Y_{big-end,small-end}$ collects the energy loss due to wall friction and losses at entry and exit; $\Delta p_{gyros}^{straight}$ is the term of fictitious force and consists of constraining force density, the centrifugal force density and a term depending on the temporal change of the rotation velocity of the reference body [16].

2.2. Preliminary design of the DPO gallery

At the beginning, two specific analyses have been carried out. In the first analysis, the baseline configuration of the conrod has been simulated. In particular, the DPO gallery is absent, and the oil supply of the small-end is ensured by a hole located at its top and aligned with the

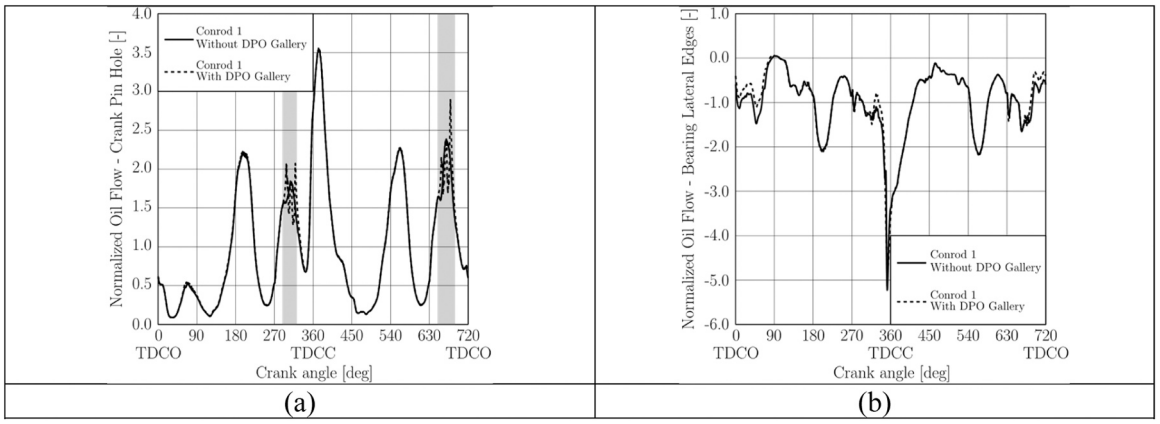

Fig. 10. Normalized oil flow in the big-end bearing of the conrod with the preliminary DPO gallery: (a) crank pin hole; (b) bearing lateral edges.

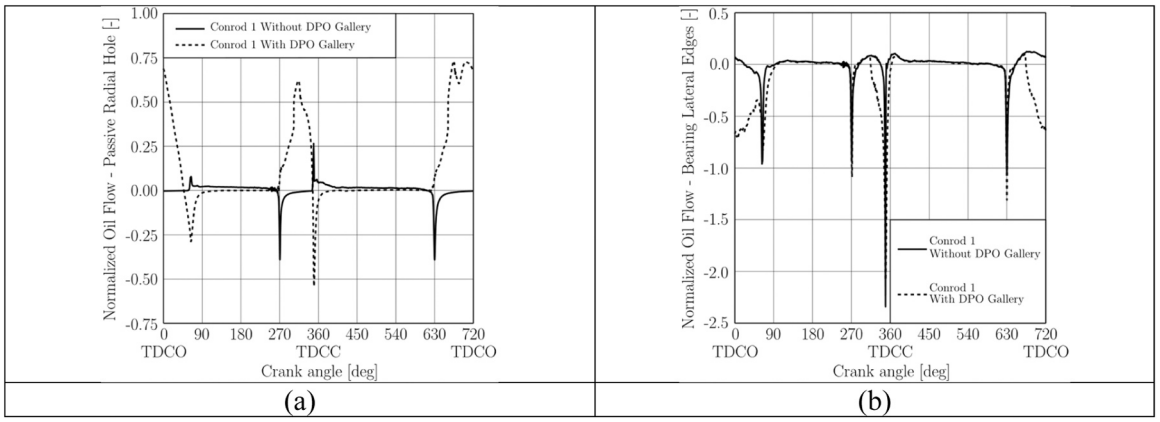

Fig. 11. Normalized oil flow in the small-end bearing of conrod 1 with and without the preliminary DPO gallery: (a) passive radial hole/gallery hole; (b) bearing lateral edges.

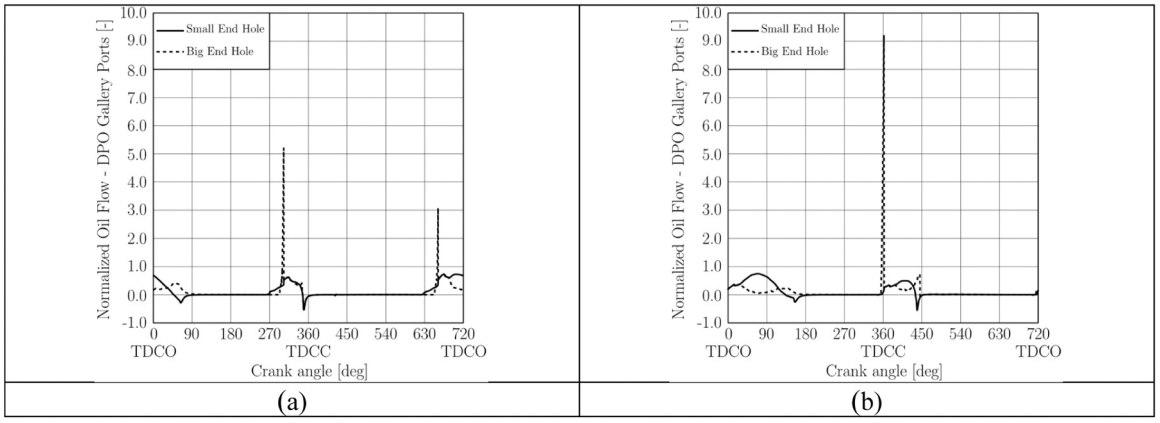

Fig. 12. Normalized oil flow through the preliminary DPO gallery ports: (a) conrod 1; (b) conrod 3.

conrod axis, see Fig. 7(a). In the second analysis, a preliminary design of the DPO gallery has been introduced, see Fig. 7(b), and its effect has been studied by comparing the results with those of the first simulation.

In particular, the preliminary configuration chosen corresponds to that of Fig. 1(e). This arrangement of the DPO is usually adopted for the purpose of limiting the effects of the presence of the holes on the generation of correct hydrodynamic support. In fact, the hole in the big-end is not located in the centre of the upper half bearing, where the maximum hydrodynamic pressure is registered when the crank mechanism is at the top dead centre during combustion (TDCC) [25,26], and, similarly, the hole in the small-end is not located in the centre of the lower portion of this interface, where again the maximum hydrodynamic pressure is registered at TDCC [27].

Nevertheless, the engine under consideration is a four-cylinder V-Type engine, and identical conrods should be fitted to both engine banks to reduce assembly errors. Consequently, each crank pin is coupled with two connecting rods reversed to each other and the adopted DPO gallery results therefore asymmetrically positioned when looking at the two conrod serving the two banks. The connecting rod small-end and big-end bearings of the two banks can therefore have different oil flow rates due

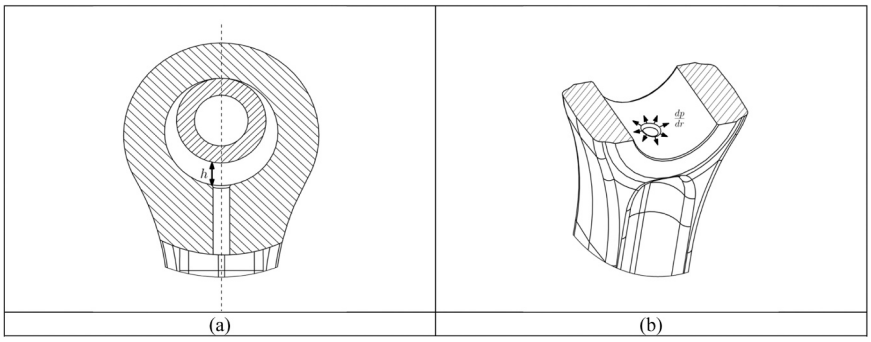

Fig. 13. Parameters governing the oil flow through the DPO gallery: (a) oil film thickness; (b) radial pressure gradient.

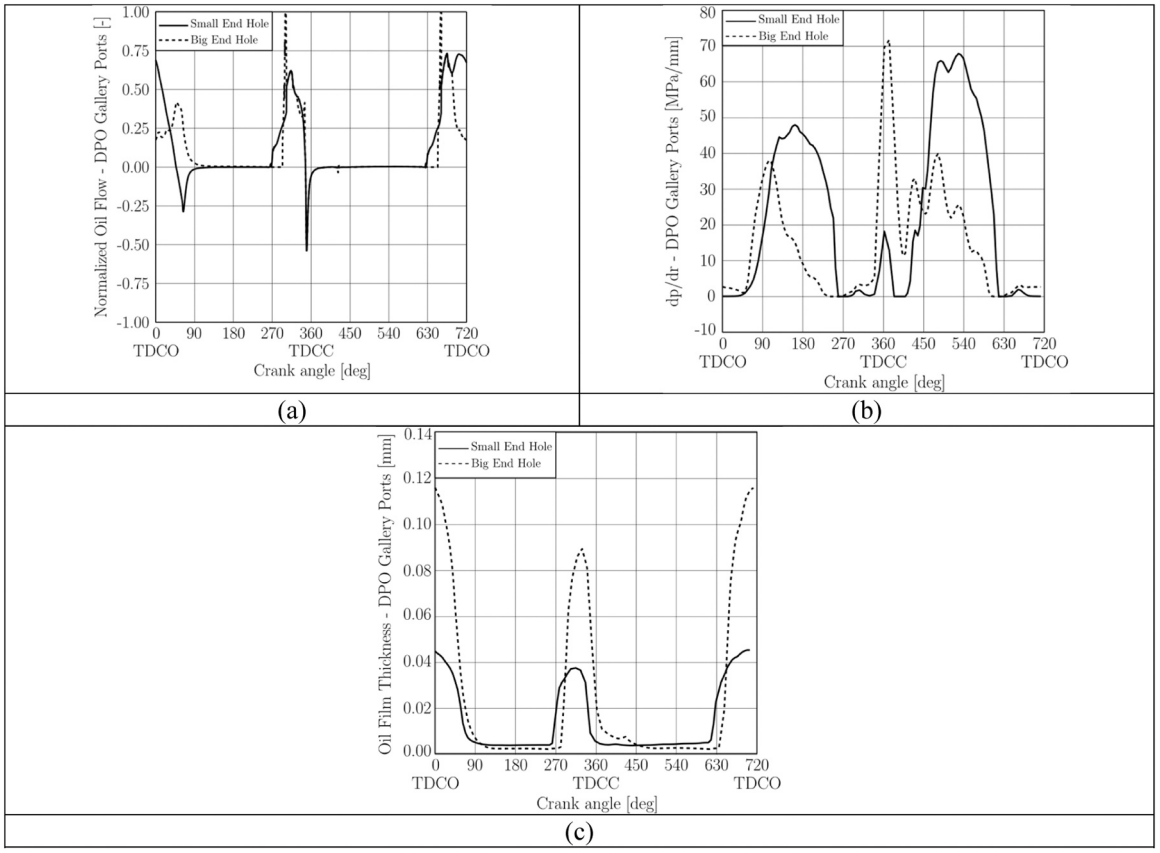

Fig. 14. Connecting rod 1: (a) DPO gallery normalized oil flow profile; (b) dp/dr profile; (c) oil film thickness profile in correspondence of the DPO galley communicating holes.

to this not-specular configuration and a different behaviour in terms of hydrodynamic effects and wear could be registered for the two bearings, complicating the assessment of the reliability of these components.

3. Multibody results: effect of the preliminary DPO introduction

In analysing the results of these first multibody simulations, the authors mainly focused on two aspects: a) oil flow balance in the big-end and small-end hydrodynamic bearings; b) tribological behaviour of these interfaces in terms of hydrodynamic pressure and asperity contact pressure. These two aspects are addressed in dedicated sections in the following.

3.1. Oil flow balance

First of all, the results relating to the connecting rod without the DPO gallery have been collected and discussed. The results referring to the connecting rod equipped with the DPO gallery are reported and this effect has been quantified by comparing these results with those from the original design. This discussion has been accomplished by monitoring the inlet/outlet oil flow curves of both the big-end and small-end bearings. The authors aimed to determine the amount of oil supplied to the bearings from the feed holes and that lost through the bearing edges during a single engine cycle.

Please note that all the values referring to oil flows have been normalized with respect to the average flow of oil out of the crankshaft feeding hole in the original case without the DPO gallery for confidentiality reasons.

3.1.1. Oil flow balance: conrod without the DPO gallery

Fig. 8(a) depicts the normalized volumetric oil flow rate feeding the big-end bearing from the hole in the crankpin, while Fig. 8(b) shows the

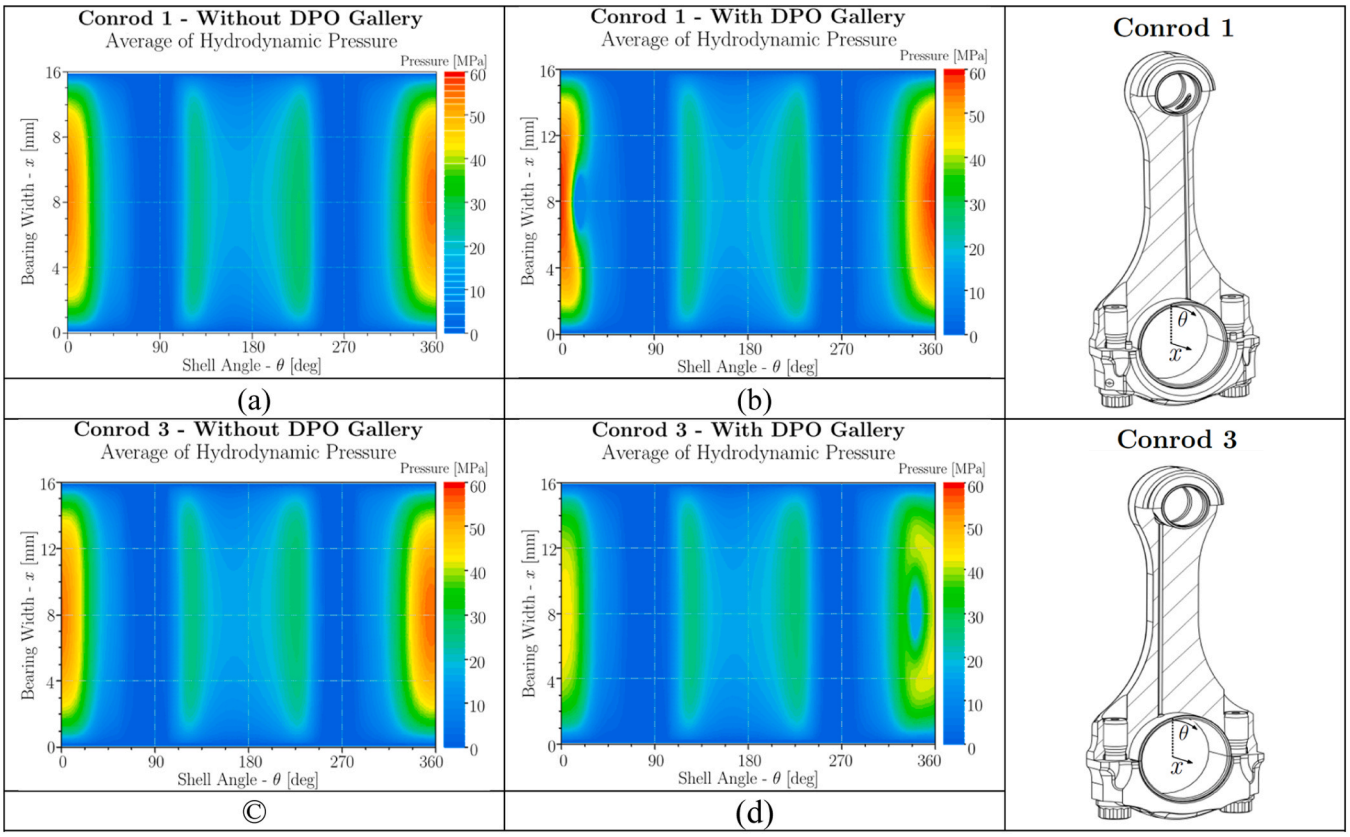

Fig. 15. Comparison between the average hydrodynamic pressure distributions in the big-end bearings of conrod 1 and 3 in the case without and with DPO gallery.

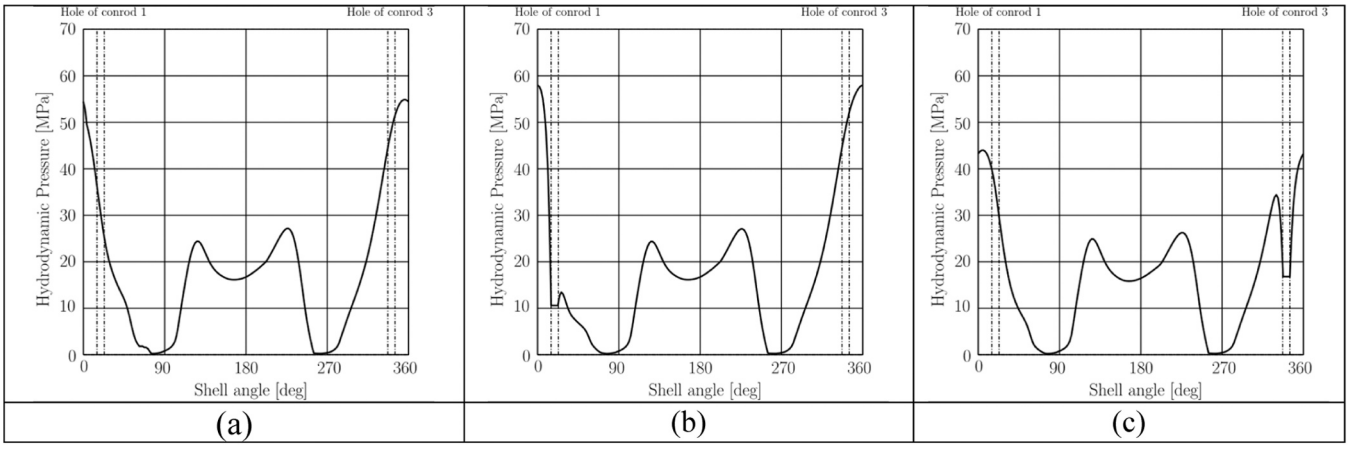

Fig. 16. 2D mid-section of the average hydrodynamic pressure of big-end bearings: (a) conrod 1 without DPO gallery; (b) conrod 1 with DPO gallery; (c) conrod 3 with DPO gallery.

normalized volumetric flow rates disposed of by the bearing side edges for both conrods 1 and 3.

It is evident that the oil which passes through the connecting rod bearings of the two banks has the same profile, only shifted by the corresponding thermodynamic angle between the two cylinders, i.e. 90° CA. As a result, the average flow of oil into the bearing is the same in both connecting rods. Furthermore, the total amount of oil exiting the side edges of the big-end during an entire engine cycle is obviously equal to the total amount of oil entering the bearing through the crankpin feed hole, see Table 3.

As regards the connecting rod small-end, Fig. 9(a) shows the normalized volumetric flow rate entering from the passive hole located on its top while Fig. 9(b) shows the normalized flow exiting the lateral edges of the connecting rod small-end 1 and 3. The same considerations valid for the big-end can also be made for the small-end in terms of both instantaneous and average flow rate, see Table 4.

3.1.2. *Oil flow balance: conrod equipped with the preliminary DPO gallery*

Moving on to the results of the second multibody simulation, Figs. 10 and 11 compare the baseline conrod 1 normalized oil flow (solid line) with that obtained adopting the preliminary DPO gallery design (dashed line). The results for conrod 3 provide limited additional information and have therefore been omitted for the sake of brevity.

Fig. 10 refers to the big-end. In particular, Fig. 10(a) shows the

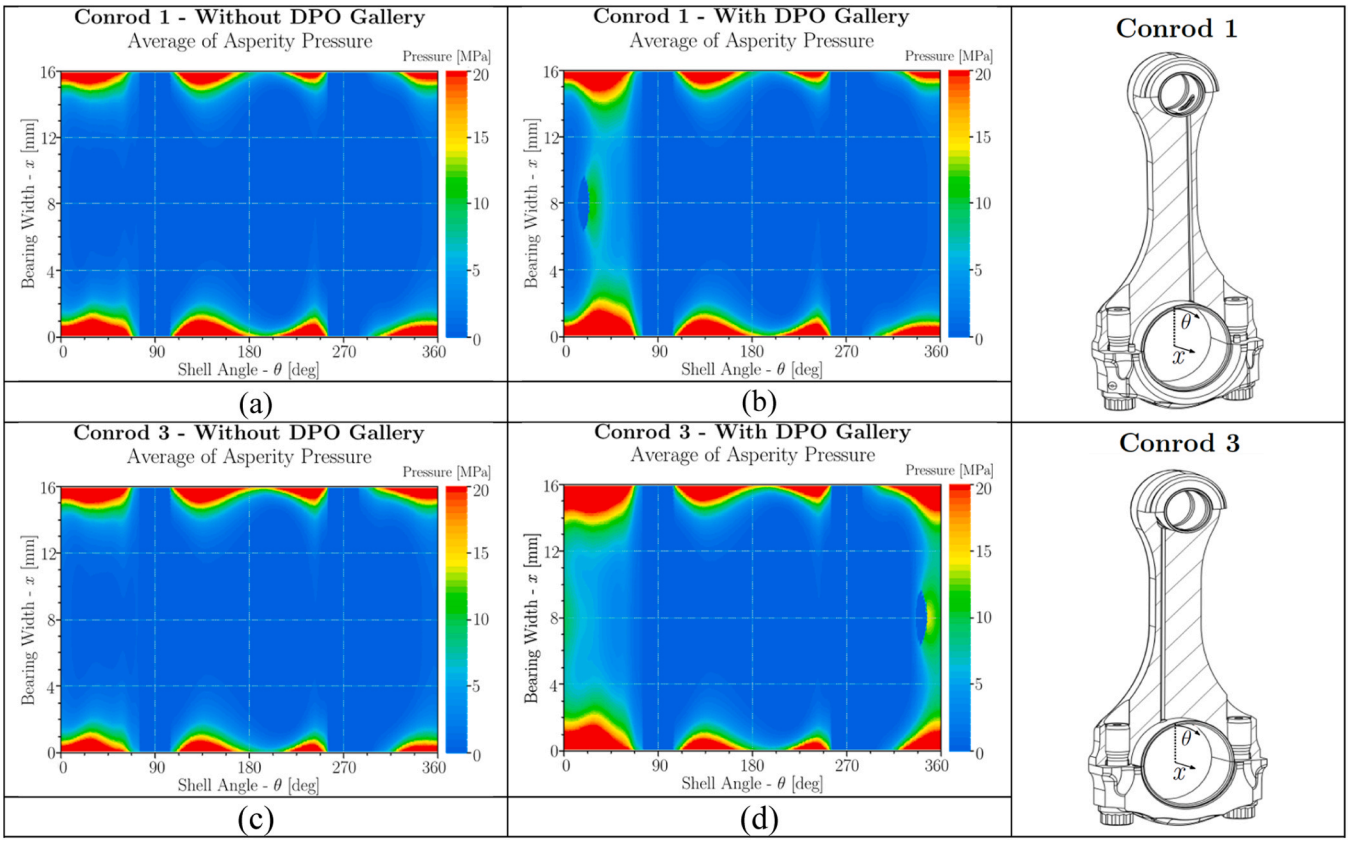

Fig. 17. Comparison between the average asperity pressure distributions in the big-end bearings of conrod 1 and 3 in the case without and with DPO gallery.

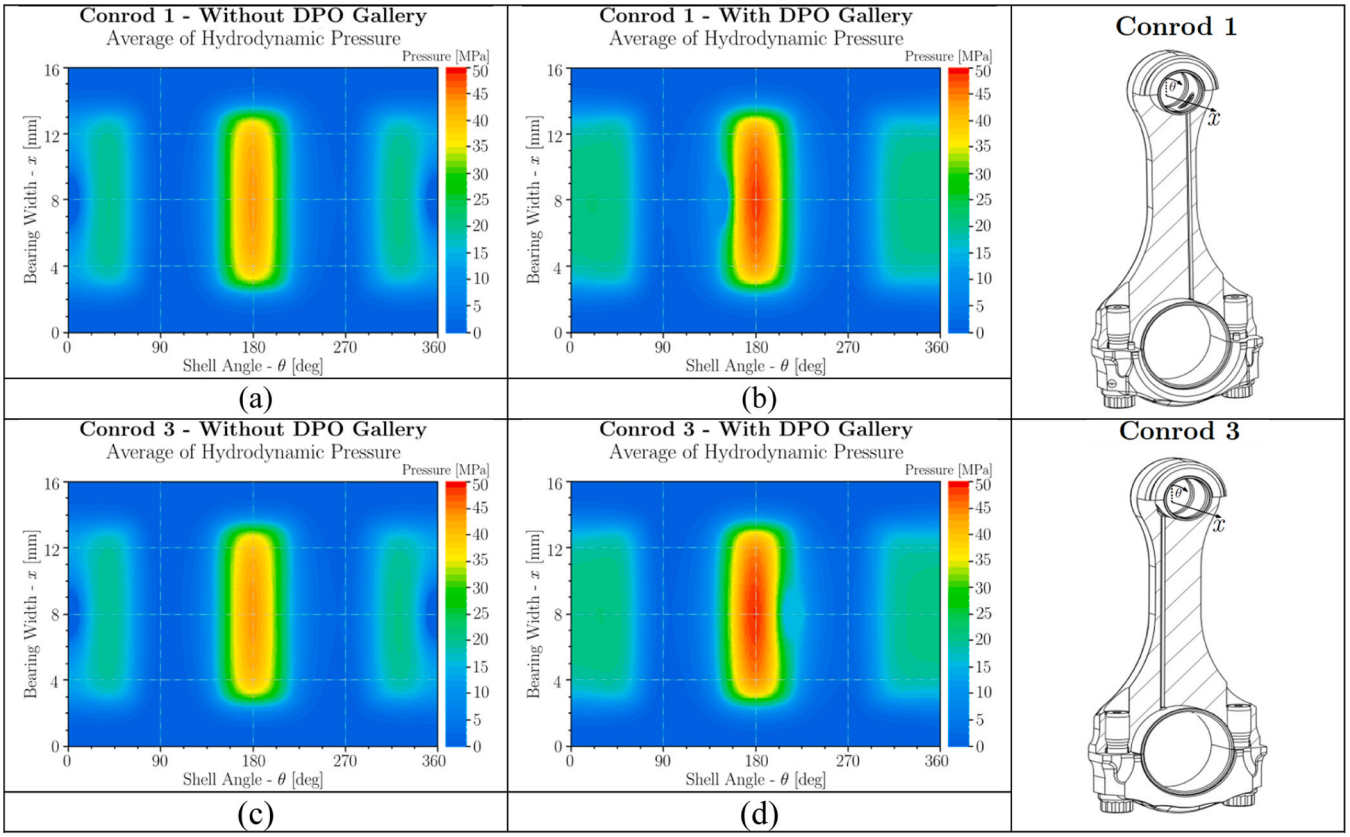

Fig. 18. Comparison between the average hydrodynamic pressure distributions in the small-end bearings of conrod 1 and 3 in the case without and with DPO gallery.

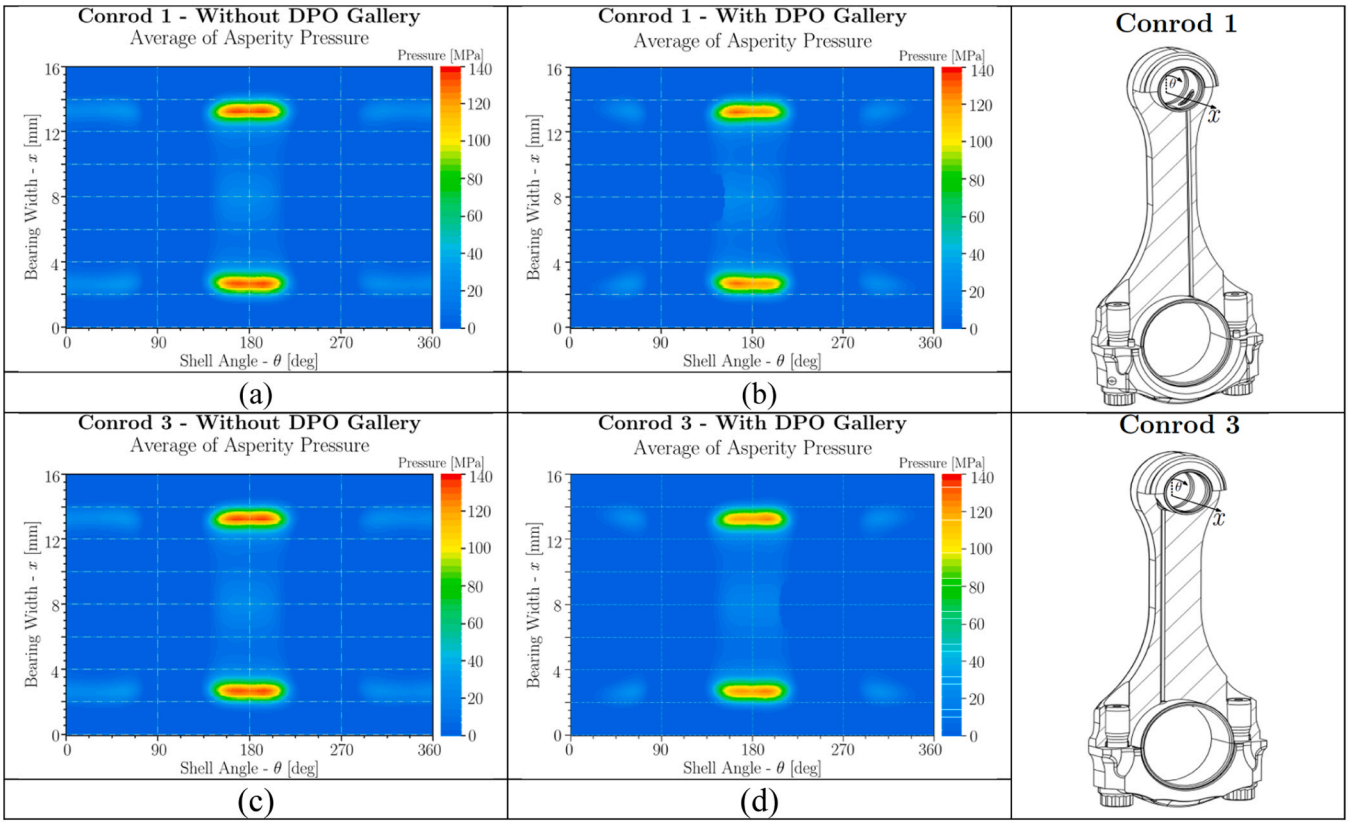

Fig. 19. Comparison between average asperity pressure distributions in the small-end bearings of conrod 1 and 3 in the case without and with DPO gallery.

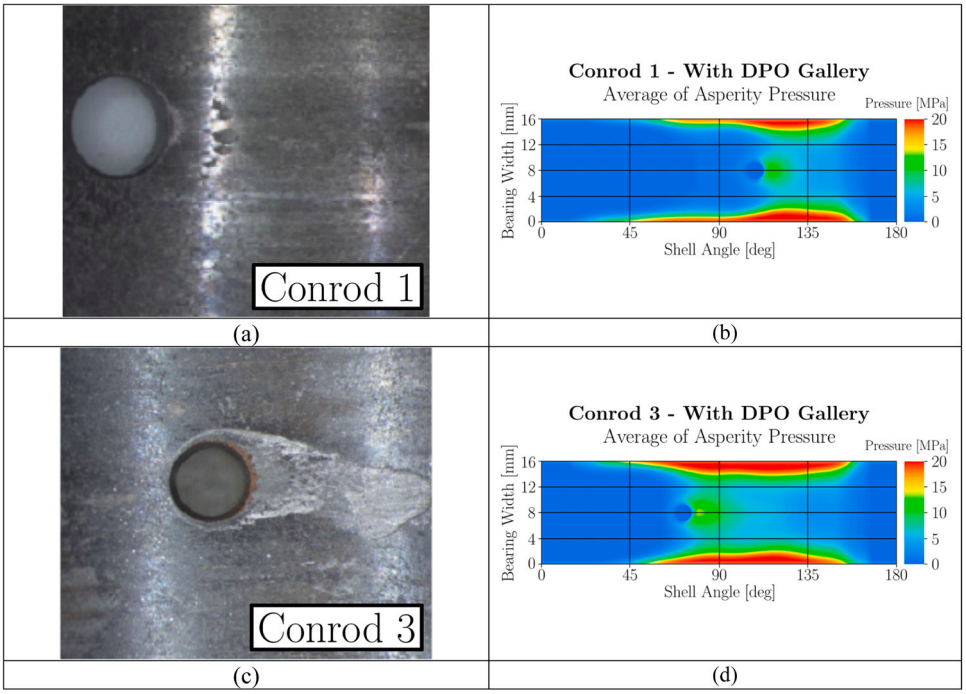

Fig. 20. Conrod big-end bearing: experimental wear evidence compared to numerical results.

normalized oil supply from the crank pin hole. The curves have similar trends except for the crank angles where the crankpin hole is aligned with the big-end hole (see grey bands). Fig. 12(b) illustrates the normalized oil flow exiting the edges. The trend is similar, however the outgoing flow from the lateral edges is lower in the case of the connecting rod with the DPO gallery, since a part of the incoming flow goes into the DPO gallery.

Fig. 11 compares the normalized oil flow rate referred to the small-end. In this case, the differences are evident. Fig. 11(a) shows the normalized flow of oil entering the small-end. The adoption of the DPO

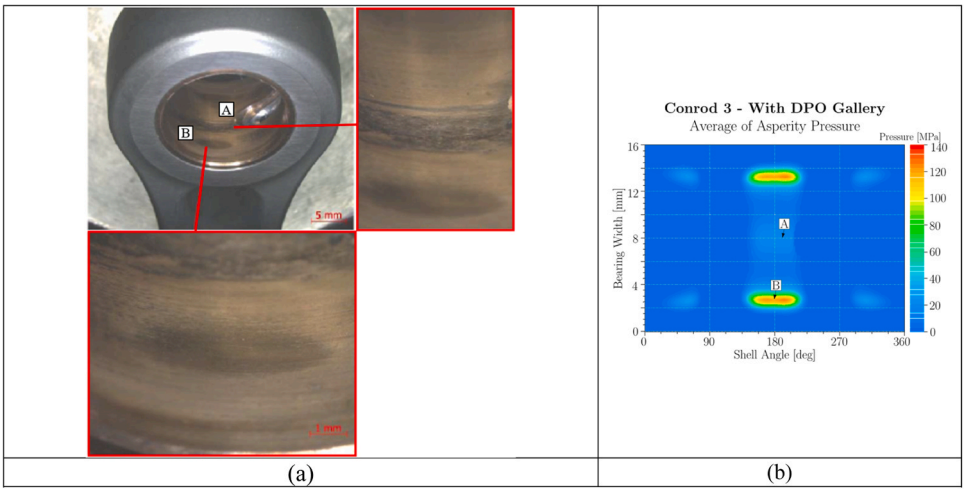

Fig. 21. Conrod small-end bushing: experimental wear evidence compared to numerical results.

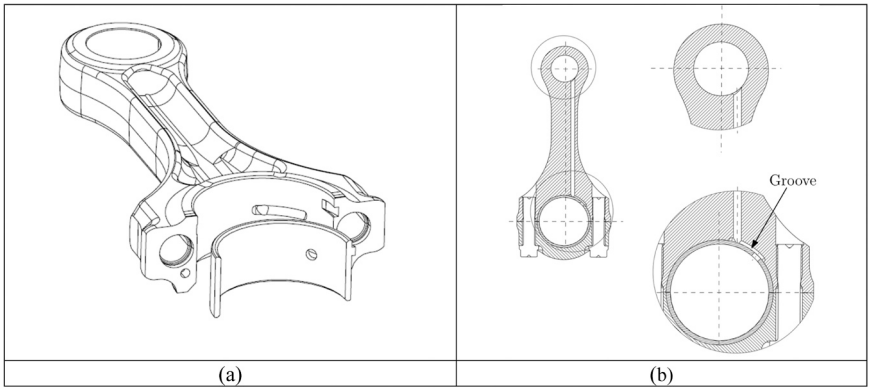

Fig. 22. Drawing of new DPO gallery configuration.

gallery greatly increases the oil supply. As a result, the oil exiting the edges also differs significantly, see Fig. 11(b).

Fig. 12 shows the normalized oil flow affecting the DPO gallery of connecting rod 1, Fig. 12(a), and connecting rod 3, Fig. 12(b). The solid black lines refer to the small-end hole; positive values identify an oil flow exiting the DPO gallery and entering the small-end. The dotted lines concern the connecting rod big-end hole; positive values identify an oil flow exiting the connecting rod big-end and entering the DPO gallery. Focusing on the diagrams, the behaviour of the two connecting rods is not identical. Indeed, an asymmetric DPO configuration was designed, see Fig. 7(b). However, the amount of the overall oil that flows out of the crankpin hole and reaches the small-end is marginally affected by this asymmetry, see Table 4.

Continuing to observe the curves, the flow peaks entering the galleries on the big-end side are caused by the alignment of the galleries with the crank pin feed hole. In particular, a significant peak in oil flow occurs when the two holes are facing each other and the pressure on the shaft side is greater than that in the DPO gallery. The difference in peak height between the two connecting rods is due to the different pressure difference between the hole in the connecting rod gallery and the hole in the crankshaft gallery. Conversely, if the connecting rod bore overlaps with the shaft bore when there is high hydrodynamic pressure in the DPO gallery, there is a backflow of oil into the shaft. In both of these cases, the oil flow in the channel is governed by the different pressures between the DPO gallery and the crankshaft oil supply.

However, additional considerations can be made to further interpret the results of Fig. 14 at those times when the crank pin oil supply hole is not facing the gallery. In this case, the flow rate through the holes serving the DPO gallery can be estimated using the following equation:

$$Q = -\frac{h^3}{12\mu}\frac{\partial p}{\partial r}2\pi r \tag{2}$$

where h is the oil film thickness around the hole, see Fig. 13(a), $\partial p/\partial r$ is the pressure gradient in the radial direction across the hole, see Fig. 13 (b), μ is the viscosity of the oil and r is the radius of the hole. Therefore, the two most important parameters to monitor during the analysis governing the oil flow through the DPO gallery are the instantaneous oil film thickness and pressure gradient around the hole.

In this sense, Fig. 14(a) depicts the normalized oil flow in the DPO gallery, Fig. 14(b) the $\partial p/\partial r$ around the hole and Fig. 14(c) the thickness of the oil film in correspondence with the gallery of connecting rod 1. From the comparison of the three curves, it emerges that what most influences the transport of the oil in the DPO gallery is the instantaneous height of the oil film, while the pressure gradient is not a determining parameter. In fact, a high quantity of oil passes through when a thick film of oil is present around the DPO openings. In contrast, when there is significant hydrodynamic pressure around the holes there is a contemporary limited oil flow and there is almost no oil passage.

A final discussion can be then made about the results collected in Table 3 and Table 4. In particular, Table 3 summarizes the normalized average oil flows that develop in the conrod big-end bearings. First and foremost, the table shows that, despite having a non-symmetrical configuration, the behaviour of the two connecting rods in terms of oil flows is almost the same. Getting into specifics, in the case with the DPO gallery, a 7 % higher amount of oil flow is required from the crankshaft

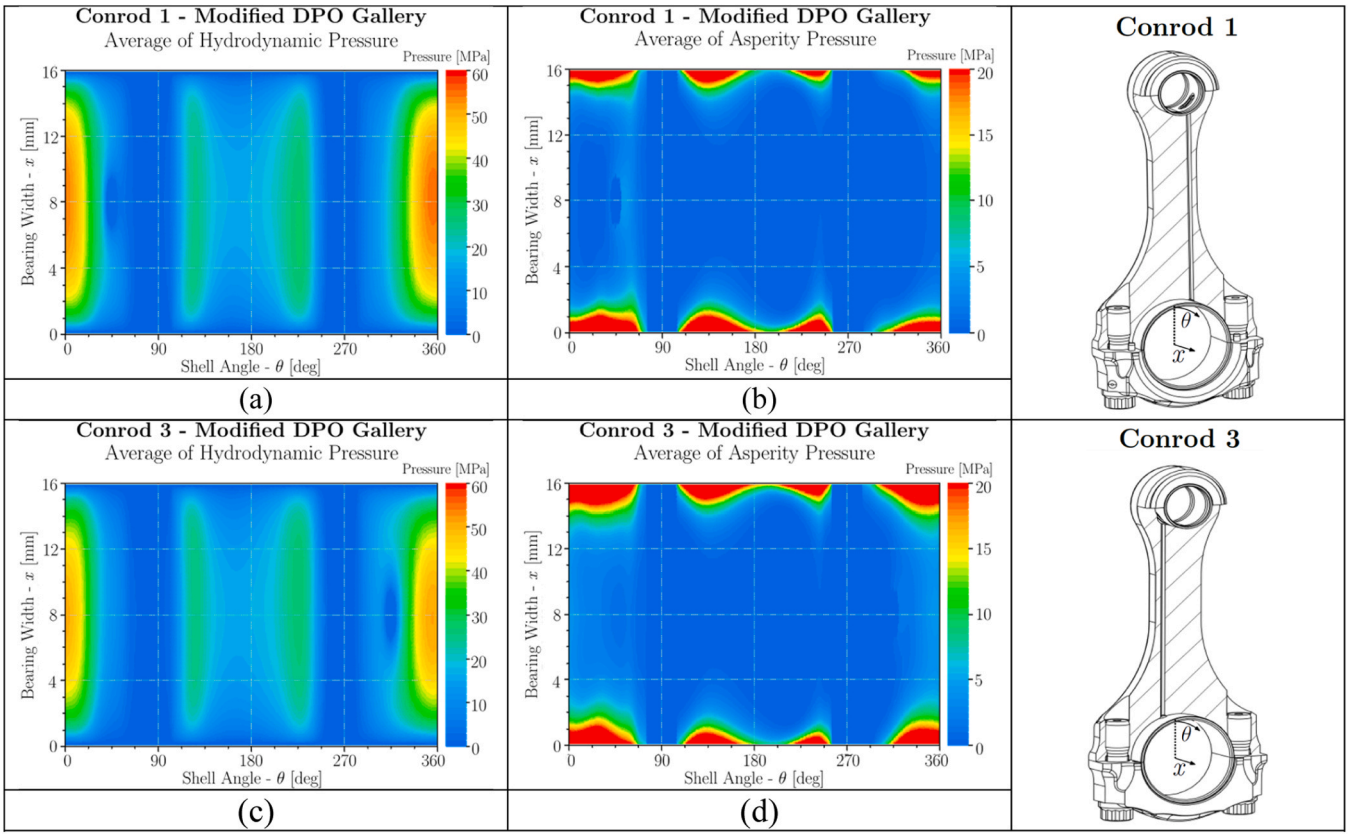

Fig. 23. Comparison between the average hydrodynamic pressure and the average asperity contact pressure distributions in the big-end bearings of conrod 1 and 3 in the case with the modified DPO gallery.

hole. This extra flow almost entirely goes straight into the DPO gallery and reaches the conrod small-end, partially for the "holes alignment" phenomenon and partially for the mechanisms involved in the discussion of Fig. 14. Table 4 summarizes the normalized average oil flows that develop in the bushing on the connecting rod small-end. In practice, the oil supply increases more than 25 times following the installation of the DPO gallery compared to the initial case equipped with passive holes.

From this discussion it can be concluded that the introduction of the DPO gallery significantly increases the quantity of oil that reaches the small-end bushing, possibly improving its hydrodynamic behaviour, keeping the quantity of oil remaining in the big-end bearing almost unchanged, potentially not jeopardizing its behaviour, at least in terms of oil flow rate processed.

3.2. *Tribological behaviour of the conrod bearings*

Fig. 15 compares the distribution of the average hydrodynamic pressure over the entire engine cycle on the big-end bearing obtained for the two different connecting rod configurations. In the simulation without the DPO gallery, the tribological behaviour of the two connecting rods installed in the two engine banks is similar. With the adoption of the DPO gallery, the configuration is no longer symmetrical, even if the oil flows are not so dissimilar from each other, see Table 3.

Referring to the coordinate system defined in the inset of Fig. 15, the DPO gallery hole is located slightly after 0 degrees for connecting rod 1, and just before 360 degrees for connecting rod 3. Figure 16 shows a 2D mid-section of the big-end average hydrodynamic pressure distributions shown in Fig. 15(a), (b), and (d).

Comparing Fig. 16(a) with Figs. 16(b) and 16(c), it can be appreciated how the presence of holes serving the DPO gallery alters the local hydrodynamic pressure distribution. In particular, the vertical dotted lines of Fig. 16(a) identify the positions of the DPO gallery holes of both connecting rods 1 and 3 when superimposed on the hydrodynamic pressure obtained from the case of conrod 1 without DPO gallery. We can notice that, for conrod 1, the hydrodynamic pressure is disrupted in a position close to the outer border of the high hydrodynamic pressure region, where the pressure has an average value of approximately 34 MPa. Consequently, a limited local modification of the pressure profile is observed in this region in Fig. 16(b), see also Fig. 15(b). Furthermore, Fig. 17 shows the distribution of the average asperity contact pressure over the entire engine cycle on the big-end bearing obtained for the two different connecting rod configurations. In particular, Fig. 17(b) shows a non-zero asperity contact pressure region near the “right” side of the DPO gallery hole border of conrod 1, clearly absent in the original configuration of Fig. 17(a), promoted by the perturbation induced by the presence of the hole.

For conrod 3, however, the hydrodynamic pressure is disrupted in a position close to the region of maximum hydrodynamic pressure, where the pressure has an average value of approximately 48 MPa. Consequently, a deeper local modification of the pressure profile is appreciable in this region in Fig. 16(c), see also Fig. 15(d). Furthermore, a higher asperity contact pressure also occurs in the hole region to compensate for the reduction of the hydrodynamic pressure promoted by the presence of the hole, see Fig. 17(d).

Focusing on the small-end results, Fig. 18 depicts the average hydrodynamic pressure distribution over the entire engine cycle for the two different simulations. It can be noted that the hydrodynamic pressure increases by 25 %, from a maximum of approximately 40 MPa in the case without the DPO gallery to a maximum of approximately 50 MPa in the case with the DPO gallery, following the increase in the oil flow entering the coupling.

Fig. 19 shows the average asperity pressure distribution for the small-end for the two simulations. The introduction of the DPO gallery led to a reduction of the maximum asperity contact pressure following

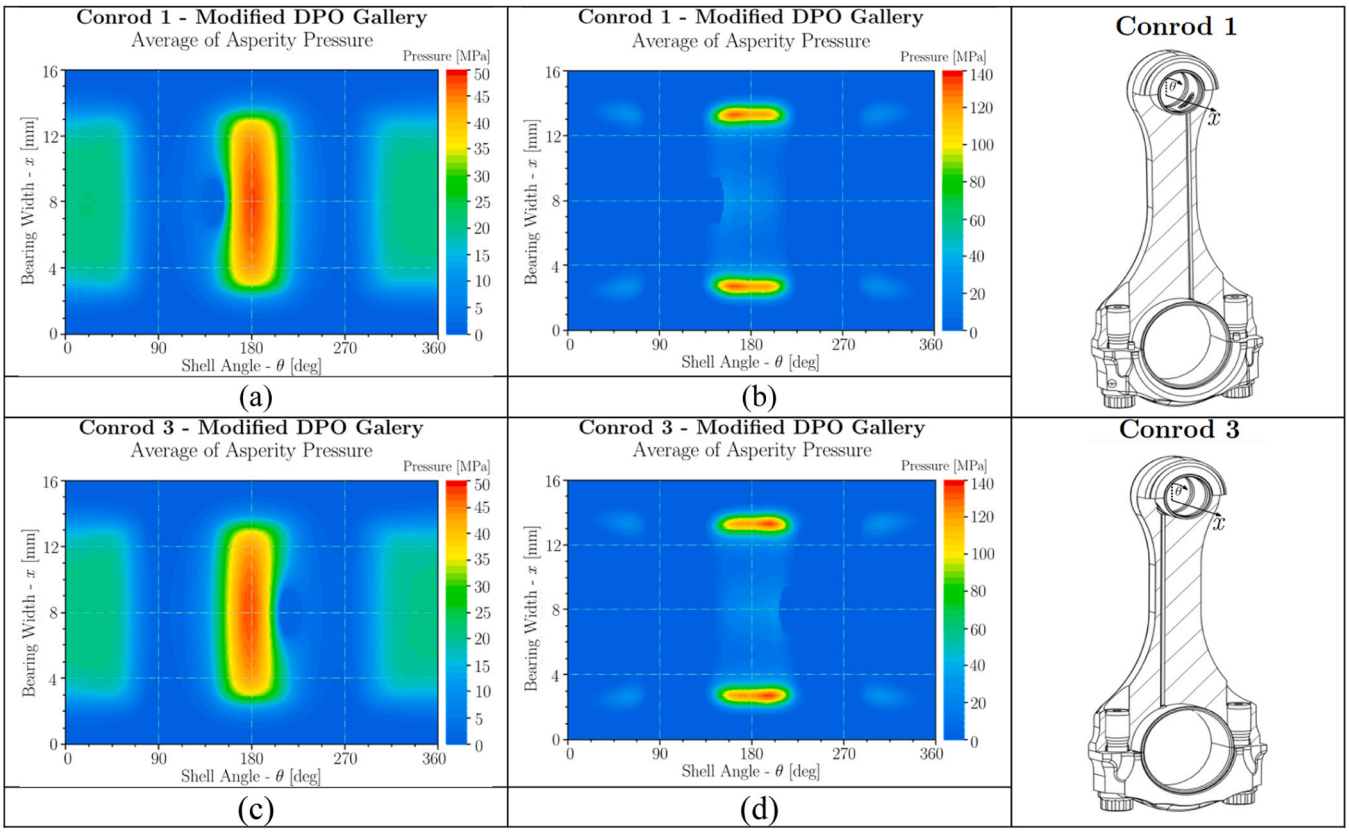

Fig. 24. Comparison between the average hydrodynamic pressure and the average asperity contact pressure distributions in the small-end bushings of conrod 1 and 3 in the case with the modified DPO gallery.

the greater hydrodynamic contribution mentioned above. However, looking at both the average hydrodynamic pressure distribution and the average asperity contact distribution, the barrel profile of the inner surface of the bushing, see Fig. 4(a), seems designed to suitably operate in correspondence with an external load insisting on the coupling higher than the one adopted in the present simulation. In fact, the extent of the region interested by a high hydrodynamic pressure is smaller than the axial extent of the bushing and the maximum asperity contact pressures promoted by the edge effect are localized slightly inside the bushing. Possible modifications of the profile could be driven following the methodology described in [28].

4. Experimental evidence

It is extremely difficult to evaluate the elasto-hydrodynamic behaviour of a sliding bearing by direct measurements from experiments. However, it is quite simple to compare the bearing wear with asperity contact distributions evaluated by the numerical analyses. Fig. 20(a) and Fig. 20(c) show the hole region of the big-end top half bearings of conrods 1 and 3 as observed following a bench test campaign on the engine under examination. It is immediately noticeable that the bearing belonging to conrod 3 shows greater wear compared to the bearings belonging to conrod 1. Specifically, localized wear is observed in conrods 1 near the hole of the DPO gallery, while more extensive wear is noted in conrods 3. This experimental evidence agrees qualitatively with the results of Figs. 17(b) and 17(d), reported here in Figs. 20(b) and 20(d) with a focus on the top half bearing for the sake of clarity.

Fig. 21(a) shows the small-end bushing of conrod 3 after the engine bench test. All the other conrods present similar wear patterns and related pictures are omitted for brevity. The experimental observations are well correlated with the numerical results. In particular, localized wear areas can be seen near the gallery hole, point A of Fig. 21(a), and towards the external edges in the lower portion of the bushing, point B of Fig. 21(a), approximately where the non-cylindrical portion of the barrel-shape profile of the internal surface of the bushing begins, see Fig. 4(a). Fig. 21(b) highlights local peaks of the average asperity contact pressure at the same locations.

These correlations demonstrate the predictive capabilities of the numerical modelling, thus allowing the authors to adopt this tool to improve the design of the DPO gallery, and possibly achieve better pressure distributions and less wear.

5. Methodology for the definition of an improved design of the DPO gallery

The original DPO gallery was designed to place the communicating holes as far away from the centre of the bearings as possible, so as not to jeopardize the critical instant of TDCC. However, structural and manufacturing constraints limit the design process, and it is not possible to position the gallery further off-centre without weakening the connecting rod. Therefore, it was not possible to position the hole in the connecting rod big-end even further from the centre of the bearing and therefore in an area such as not to significantly alter the maximum hydrodynamic pressure, see Fig. 15(d).

The new configuration of the DPO gallery was developed by introducing an additional degree of freedom into the design process. In fact, the same connecting rod configuration was used, see Fig. 1(e), and a groove was added on the inner surface of the conrod big-end, to further move the hole away from the conrod axis. Fig. 22 shows the drawing of the proposed layout. By adopting this solution, it was possible to move the hole on the bearing without moving the gallery along the connecting rod and risking weakening it [29].

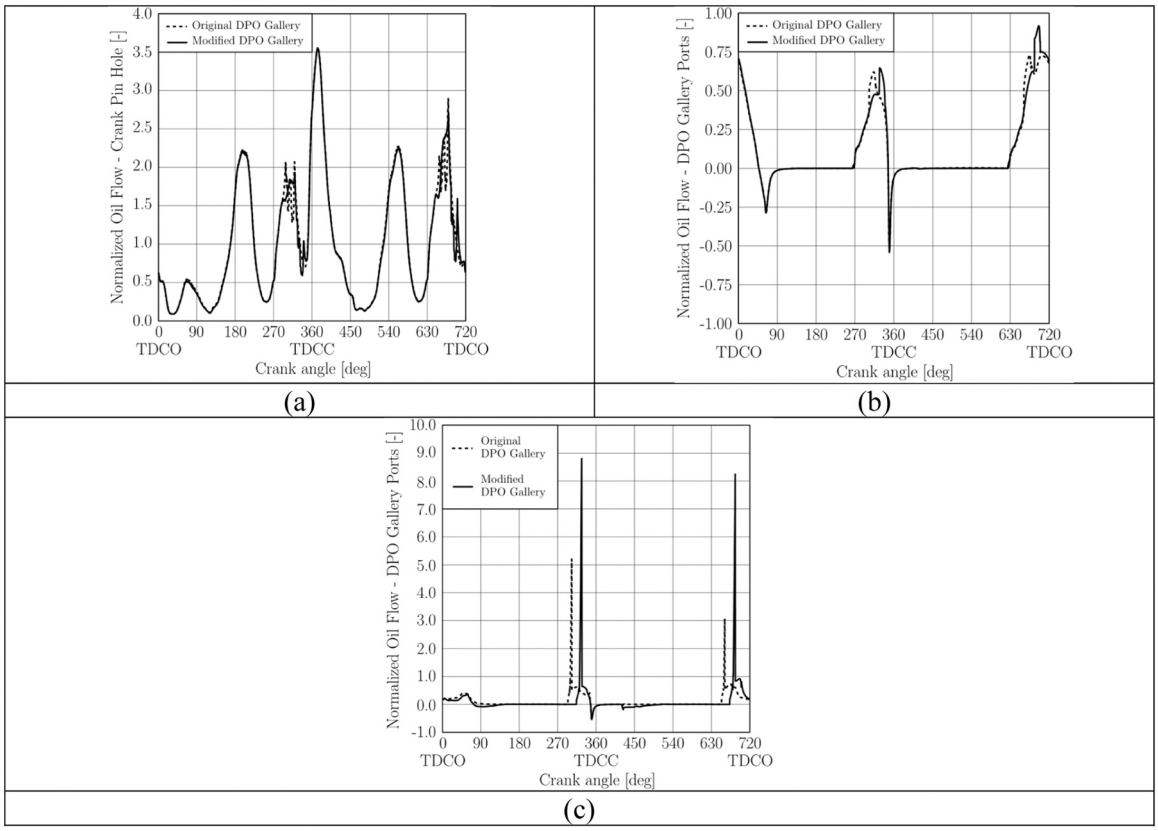

Fig. 25. Comparison of the normalized oil flow between the original and the modified DPO gallery configuration for conrod 1: (a) crank pin hole; (b) small-end DPO gallery hole; (c) big-end DPO gallery hole.

5.1. Results of the improved design for the DPO gallery

Fig. 23 shows the average hydrodynamic pressure and the average asperity contact pressure distributions for conrod 1 and 3 when the new design of the DPO is considered. The gallery hole no longer falls where the hydrodynamic pressure is high, see Fig. 15(d) and 16(c), and, for the connecting rods serving both the engine banks, the hole is now located at the border of the high hydrodynamic pressure region, see Figs. 23(a) and 23(c). Furthermore, the average asperity contact pressure is decreased, especially for conrod 3, as noticeable comparing Figs. 17(d) and 23(d).

Fig. 24 focuses on the conrod small-end. The average hydrodynamic pressure and the average asperity contact pressure are almost the same if compared to the original configuration of Figs. 18 and 19. Considering that the geometry of the conrod small-end has not been modified, this result suggests that the modification introduced in the DPO gallery design marginally affects the oil flow reaching the small-end compared to the original DPO configuration.

Specifically, a comparison of the normalized oil flows between the two DPO configurations has been collected in Fig. 25 for conrod 1 and in Fig. 26 for conrod 3. Due to the modification of the hole position on the big-end side, the peak of oil flow entering the gallery is shifted during the engine cycle, see Fig. 25(c) and Fig. 26(c). However, observing the different profiles and referring to the data collected in Tables 5 and 6 no substantial differences are found in the oil flows affecting both connecting rod bearings. Consequently, the new design could be used to mitigate the problems discussed in the previous sections and observed after the first experimental tests. Specifically, Fig. 27(a) and (c) show the same bearing locations previously depicted in Figs. 20(a) and 20(c), following a new experimental campaign of the engine under consideration and adopting the modified design of the DPO gallery. A significant improvement of the tribological behaviour can be observed as a consequence of the reduced direct contact forecasted by the simulation and here reported in Figs. 27(b) and 27(d) for the sake of clarity.

6. Conclusions

The present contribution focused on the analysis of the tribological behaviour of both the small-end and big-end bearings of a connecting rod equipped with a DPO gallery. A methodology has been proposed to identify a suitable design of the gallery for a four-cylinder V-type engine. In particular, the original configuration of the connecting rod was first analysed. The numerical results showed some issues in terms of drops in the average hydrodynamic pressure and peaks of average asperity contact pressures. These anomalies were confirmed by the experimental evidence presented.

As a result, the authors suggested a new design. The position of the gallery was kept essentially unchanged along the connecting rod shank, while the position of the hole in the big-end bearing was appropriately moved by introducing a groove on the internal surface of the conrod big-end. The new configuration was simulated, and the results showed potential improvements which were then confirmed by new experimental tests.

It is important to note that the new design was constrained by the need to obtain a connecting rod geometry suitable for both engine banks to reduce the occurrence of errors during the engine assembly phase.

Statement of originality

As the corresponding author, I Saverio Giulio Barbieri, hereby confirm on behalf of all authors that: 1) The paper has not been published previously, that it is not under consideration for publication elsewhere, and that if accepted it will not be published elsewhere in the same form, in English or in any other language, without the written

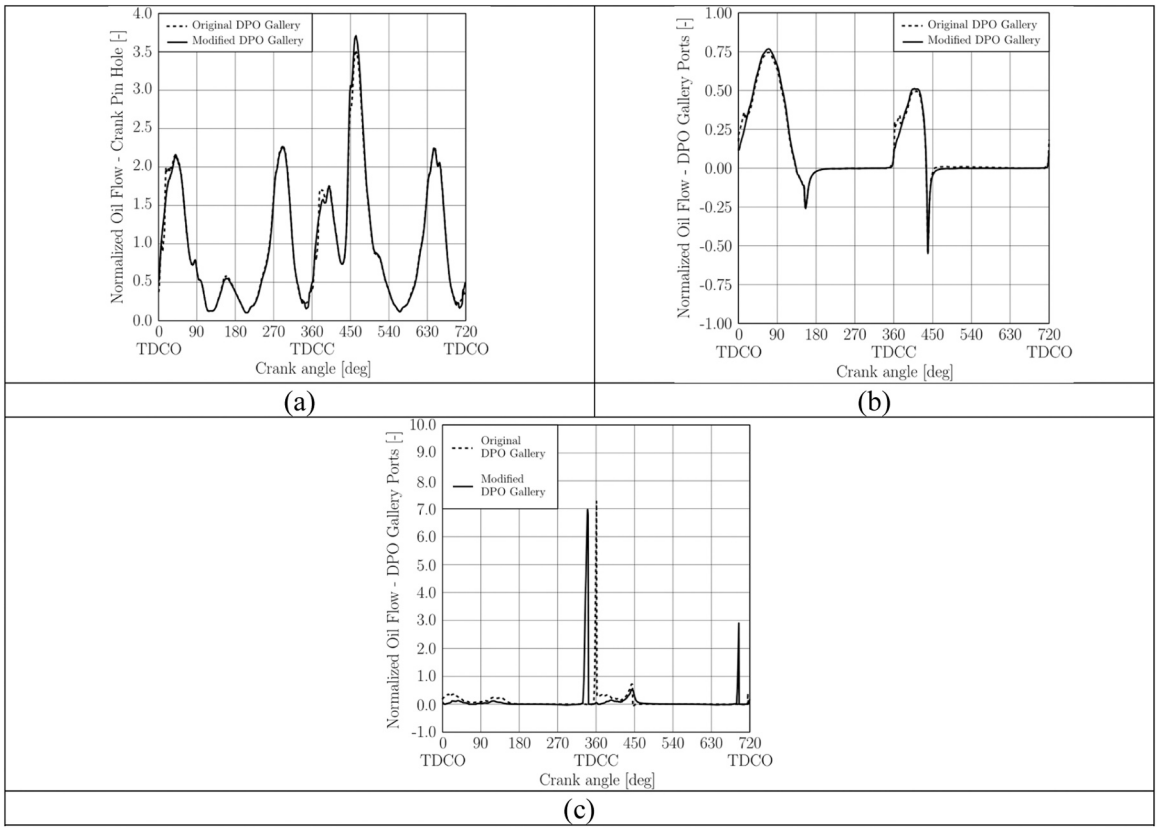

Fig. 26. Comparison of the normalized oil flow between the original and the modified DPO gallery configuration for conrod 3: (a) crank pin hole; (b) small-end DPO gallery hole; (c) big-end DPO gallery hole.

Table 5
Normalized average oil flows in the conrod big-end bearings with original and modified DPO gallery.

	Normalized average flow of oil out of the crankshaft feeding hole		Normalized average flow of oil passing directly from the crankshaft feeding hole into the DPO gallery		Normalized average flow of oil remaining in the bearing		Normalized average flow of oil passing from the bearing into the DPO gallery		Normalized average flow of oil out of the edges of the bearing	
	Original DPO gallery	Modified DPO gallery	Original DPO gallery	Modified DPO gallery	Original DPO gallery	Modified DPO gallery	Original DPO gallery	Modified DPO gallery	Original DPO gallery	Modified DPO gallery
Conrod 1	1.0710	1.1016	0.0555	0.0938	1.0155	1.0079	-0.0592	-0.0228	-0.9563	-0.9850
Conrod 3	1.0756	1.0993	0.0628	0.0852	1.0128	1.0140	-0.0569	-0.0293	-0.9559	-0.9847

Table 6
Normalized average oil flows in the conrod small-end bearings with original and modified DPO gallery.

	Normalized average flow of oil from oil supply hole		Normalized average flow of oil out of the edges of the bearing	
	Original DPO gallery	Modified DPO gallery	Original DPO gallery	Modified DPO gallery
Conrod 1	0.1147	0.1166	-0.1147	-0.1166
Conrod 3	0.1197	0.1145	-0.1197	-0.1145

consent of the publisher. 2) The paper does not contain material that has been published previously, by the current authors or by others, of which the source is not explicitly cited in the paper.

CRediT authorship contribution statement

Luigi Bianco: Writing – original draft, Software. **Andrea Ferretti:** Validation. **Michele Mazziotta:** Validation. **Valerio Mangeruga:** Data curation. **Saverio Giulio Barbieri:** Writing – review & editing, Writing – original draft, Supervision, Data curation. **Matteo Giacopini:** Writing – review & editing, Supervision, Methodology.

Declaration of Competing Interest

The authors declare that they have no known competing financial interests or personal relationships that could have appeared to influence the work reported in this paper.

Data availability

The data that has been used is confidential.

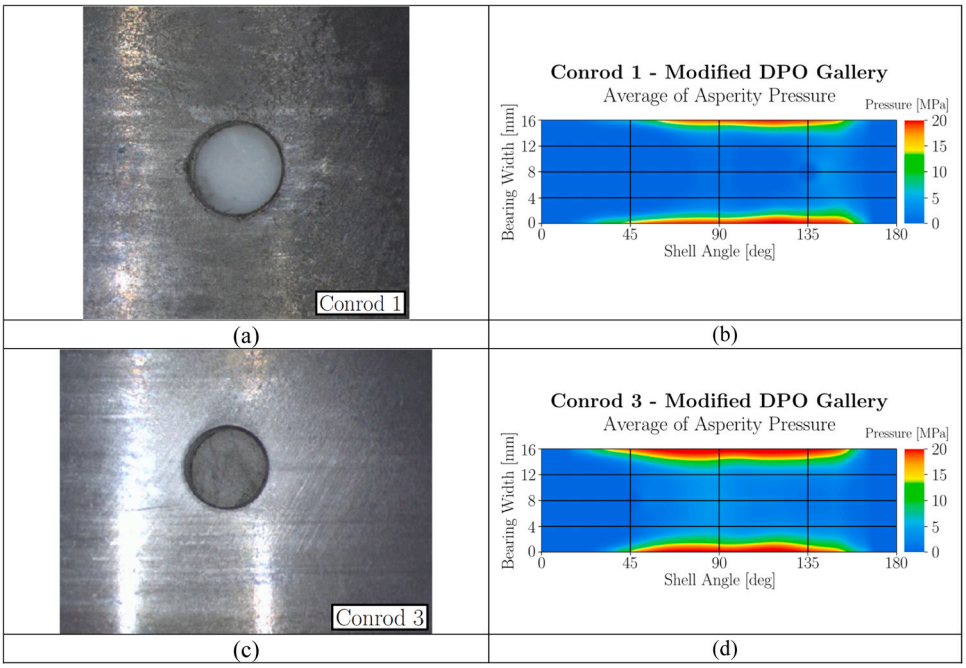

Fig. 27. Conrod big-end bearing: experimental wear evidence compared to numerical results – Modified DPO.

Acknowledgements

The authors acknowledge AVL List GmbH for the software AVL EXCITE provided for the calculation of the Multibody simulations.

References

[1] Taylor CM. Automobile engine tribology—design considerations for efficiency and durability. Wear 1998;221:1–8. https://doi.org/10.1016/S0043-1648(98)00253-1.
[2] Andersson BS. Paper XVIII (iii) company perspectives in vehicle tribology - Volvo. Tribol Ser 1991;18:503–6. https://doi.org/10.1016/S0167-8922(08)70168-8.
[3] Goenka P.K., Paranjpe R.S. A review of engine bearing analysis methods at general motors; 1992. Available from: https://doi.org/10.4271/920489.
[4] Santos NDSA, Roso VR, Faria MTC. Review of engine journal bearing tribology in start-stop applications. Eng Fail Anal 2020;108:104344. https://doi.org/10.1016/j.engfailanal.2019.104344.
[5] Okrent EH. The effect of lubricant viscosity and composition on engine friction and bearing wear. ASLE Trans 1961;4:97–108. https://doi.org/10.1080/05698196108972423.
[6] Parker RJ, Signer HR. Lubrication of high-speed, large bore tapered-roller bearings. J Lubr Technol 1978;100:31–8. https://doi.org/10.1115/1.3453110.
[7] Suzuki S., Ozasa T., Noda T., Konomi T. Analysis of con-rod big-end bearing lubrication on the basis of oil supply rate. SAE Technical Papers; 1998. Available from: https://doi.org/10.4271/982439.
[8] JASKIERNIK M, BUCZEK K, WALKOWIAK J. Simulation of the oil supply through the connecting rod to the piston cooling channels in medium speed engines. Combust Engines 2020;180:25–30. https://doi.org/10.19206/CE-2020-104.
[9] Makireddi D, Puri YM, Ghuge VD. Development of crank–connecting rod attachment for electric discharge machining of curved holes 2021:777–83. https://doi.org/10.1007/978-981-15-3639-7_93.
[10] Kang S-H, Kim J-G, Chung K-N. Prediction of transient lubricating oil flows within the connecting-rod of a diesel engine. J Mech Sci Technol 2011;25:103–9. https://doi.org/10.1007/s12206-010-1109-6.
[11] Ligier J, Ragot P. Small end conrod lubrication 2006. https://doi.org/10.4271/2006-01-1101.
[12] Du Q, Cheng Y, Ren P, Zhang Z. Optimization of crankshaft main bearing lubrication performance considering bearing profiles. J Phys Conf Ser 2020;1601:062051. https://doi.org/10.1088/1742-6596/1601/6/062051.
[13] Yin J, Liu R, Zhang R, Lv B, Meng X. A new tribo-dynamics model for engine connecting rod small-end bearing considering elastic deformation and thermal effects. Tribol Int 2023;188:108831. https://doi.org/10.1016/j.triboint.2023.108831.
[14] Craig RR, MervynCC Bampton. Coupling of substructures for dynamic analyses. AIAA J 1968;6:1313–9. https://doi.org/10.2514/3.4741.
[15] Barbieri SG, Bianco L, Mangeruga V, Giacopini M. A simplified finite element methodology for the structural assessment of an engine piston under dynamic loadings. AIP Conf Proc 2020;vol. 2309:020014. https://doi.org/10.1063/5.0033956.
[16] AVL. EXCITE power unit user manual. AVL List GmbH; 2019.
[17] Elrod HG, Adams M. A computer program for cavitation and starvation problems. In: Proceedings of the first Leeds Lyon symposium on cavitation and related phenomena in lubrication, I.M.E. 1974:37–41.
[18] Elrod HG. A cavitation algorithm. J Lubr Technol 1981;103:350–4. https://doi.org/10.1115/1.3251669.
[19] Strozzi A, Baldini A, Giacopini M, Bertocchi E, Mantovani S. A repertoire of failures in gudgeon pins for internal combustion engines, and a critical assessment of the design formulae. Eng Fail Anal 2018;87:22–48. https://doi.org/10.1016/j.engfailanal.2018.02.004.
[20] Strozzi A, Baldini A, Giacopini M, Bertocchi E, Bertocchi L. Achievement of a uniform contact pressure in a shaft–hub press-fit. Proc Inst Mech Eng C J Mech Eng Sci 2013;227:405–19. https://doi.org/10.1177/0954406212461994.
[21] Repka M, Dörr N, Brenner J, Gabler C, McAleese C, Ishigo O, et al. Lubricant-surface interactions of polymer-coated engine journal bearings. Tribol Int 2017;109:519–28. https://doi.org/10.1016/j.triboint.2017.01.017.
[22] Greenwood JA, Tripp JH. The elastic contact of rough spheres. J Appl Mech 1967;34:153–9. https://doi.org/10.1115/1.3607616.
[23] Elias E, Gibson GJ, Greenwood LF, Hunt JN, Tripp JH. The slowing of gastric emptying by monosaccharides and disaccharides in test meals. J Physiol 1968;194:317–26. https://doi.org/10.1113/jphysiol.1968.sp008410.
[24] Greenwood JA, Tripp JH. The contact of two nominally flat rough surfaces. Proc Inst Mech Eng 1970;185:625–33. https://doi.org/10.1243/PIME_PROC_1970_185_069_02.
[25] Ferretti A, Giacopini M, Dini D, Fantoni S. Experimental measurement of roughness data and evaluation of Greenwood/Tripp parameters for the elastohydrodynamic analysis of a conrod small-end/piston pin coupling. SAE Int J Adv Curr Pr Mobil 2019;2:2019. https://doi.org/10.4271/2019-24-0081.
[26] Ferretti A, Giacopini M, Mastrandrea L, Dini D. Investigation of the influence of different asperity contact models on the elastohydrodynamic analysis of a conrod smal. SAE Int J Engines 2018;11:2018. https://doi.org/10.4271/2018-01-0836.
[27] Mastrandrea LN, Giacopini M, Bertocchi E, Strozzi A, Dini D. A complete 3-D description of the elastic behavior of a piston ring and its influence on the tribological behavior of the piston ring-cylinder liner interface. Soc Tribol Lubr Eng Annu Meet Exhib 2016;2016:121–4.
[28] Bianco L, Barbieri SG, Mangeruga V, Giacopini M, Capoccia G. Influence of the thermal deformation on the lubricating performance of the piston-gudgeon pin interface in an internal combustion engine. Tribol Int 2022;174:107719. https://doi.org/10.1016/j.triboint.2022.107719.
[29] Juarez C, Rumiche F, Rozas A, Cuisano J, Lean P. Failure analysis of a diesel generator connecting rod. Case Stud Eng Fail Anal 2016;7:24–31. https://doi.org/10.1016/j.csefa.2016.06.001.